REPRESENTATION OF HYPERSONIC GLIDE VEHICLES AS FLUCTUATING RADAR TARGETS

Jonathan Pinto[1]*, Neil Lindsay Whyman[2], Hugh Griffiths[3]

[1]Electronic Systems, BAE Systems Digital Intelligence, West Hanningfield Rd, Gt. Baddow, Chelmsford, UK.
[2] UK Ministry of Defence (MoD), Main Building, Horse Guards Ave, Whitehall, London SW1A 2HB, UK.
[3]Electronic and Electrical Engineering, University College London, Malet Place, London, WC1E 7JE, UK.

*jon.pinto@baesystems.com

Keywords: RCS, HYPERSONIC GLIDE VEHICLE, SWERLING DISTRIBUTION, FLUCTUATING TARGET.

Abstract

The monostatic RCS of a generic Hypersonic Glide Vehicle (HGV) is presented at S-band and is derived using a Physical Optics (PO) based simulation approach. Target RCS histograms are then produced and used to generate a custom statistical distribution which is subsequently compared against the conventional Swerling models associated with representation of target fluctuation when using the Radar Range Equation (RRE). The accuracy of the Swerling models for this particular target type and frequency band is subsequently discussed.

1. Introduction

Hypersonic Glide Vehicles (HGVs) offer unique challenges, in terms of detection and tracking, for ground based radars. This results from their potentially high radial velocity with respect to the radar, unpredictable flight profile, and low altitude (in the latter case relative to conventional Re-entry Vehicles (RVs) following a ballistic trajectory). In evaluating the effectiveness of new and existing radars in detecting/tracking these vehicles, a radar-range equation based model is invariably constructed. In these models, HGV target RCS fluctuations, and so corresponding variations in the amplitude of the voltage signal in the detector and, ultimately, the probability of detection (P_d), are represented using one of the ubiquitously applied set of distributions postulated by Peter Swerling in 1954 [1]. That work built upon prior analysis by Marcum, [2]. This paper reports the monostatic Radar cross section (RCS) of a generic HGV and subsequently derives a custom statistical distribution for a manoeuvring vehicle presenting a range of target aspect angles. This is then used to explore whether this target type remains well represented by a Swerling model. S-band frequencies were chosen to represent illumination of the target by a Multi-Function Radar. There is ongoing interest in S-band radars for general Ballistic Missile Defence (BMD) applications, since the frequency range offers a good compromise between range and resolution.

2. The RCS Model

HGVs vary considerably in size depending upon their design requirements, particularly the size and mass of the payload. However, they must all fit within the diameter of their respective boost vehicles which is often a Medium, Intermediate or Intercontinental Ballistic Missile (MRBM/IRBM/ICBM), examples of which are given in [3] and [4]. These, in turn, are generally dictated by launch tube diameter if associated with an existing platform. A geometry was constructed that was broadly representative of existing in-service systems [5], [6], and based on a shape already widely reported in the public domain [7]. A maximum width consistent with existing and proposed ICBMs such as Russia's RS-18A 'Stilletto and RS-28 'Sarmat' suggests a maximum diameter of 3m [8]. The image from [7] is shown in Fig. 1.

Fig. 1 Representation of generic boost-glide vehicle (HGV) from [7].

Given a vehicle diameter of 3m, the remaining dimensions were estimated by photogrammetry to be:
- Length – 5.1m.
- Height (base to fin tip) – 1.06m.
- Nose radius – 0.1m.

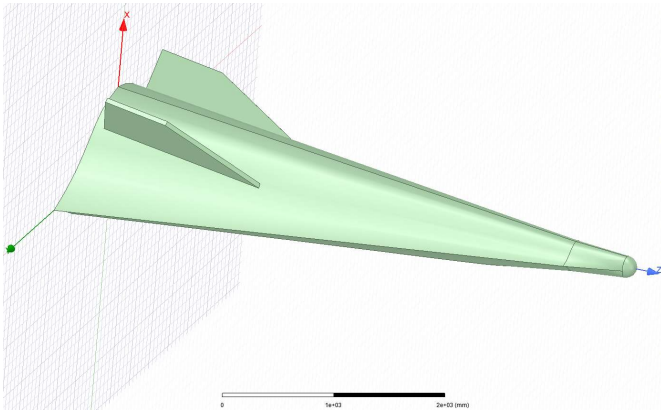The resultant geometry, as represented in Ansys' HFSS PO solver is shown in Fig. 2, Fig. 3 and Fig. 4.

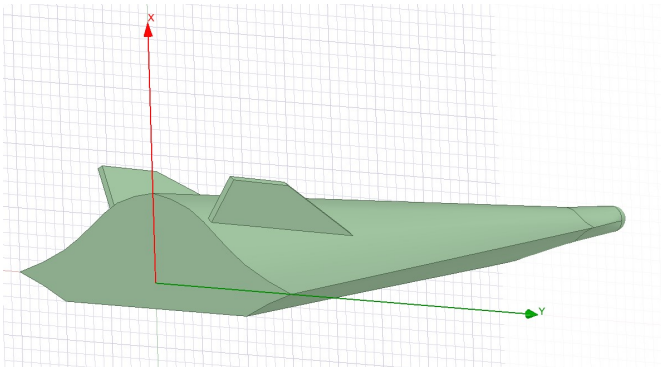**Fig. 2 Front quarter view of HGV representation in PO solver.**

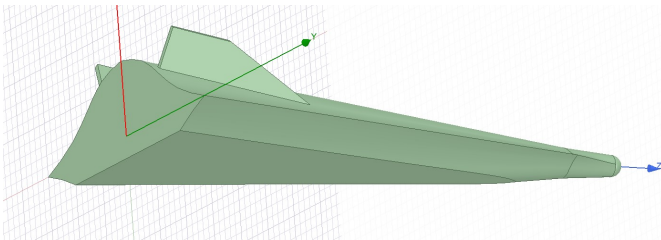**Fig. 3 Upper three quarter view of geometry in PO solver.**

Fig. 4 Lower three quarter view of geometry in PO solver.

The vehicle was assumed to be a Perfect Electrical Conductor (PEC). This is likely to be a reasonable approximation at S-band. Skin materials are generally similar to those used in more conventional RV's due to the need for thermal protection or ablation, typically consisting of carbon ceramic composites [9]. Additionally, vehicles are also generally well screened electrically in order to meet Nuclear Electromagnetic Pulse (NEMP) requirements.

Under certain circumstances, when operating endo-atmospherically (i.e. at an altitude below the Karman Line of around 100km), it is possible that plasma effects, from aerodynamic heating of the air passing over the body, may have an impact on the overall RCS. However, work undertaken as part of a previous study [10], suggests that the plasma and collision frequencies result in an ionised region

with a dispersive (frequency dependent) conductivity which, although significant at HF, VHF and low UHF frequencies, can be neglected at L-band and above.

An older version (2019, R2) of HFSS was used which did not incorporate the SBR+ solver available in the most recent versions. Shadowing and diffraction effects, via the Physical Theory of Diffraction (PTD) were included, but not surface travelling waves or other 'second order' phenomena. The surface mesh applied consisted of simple triangular surface patches rather than curvilinear elements. A relatively high mesh density equal to around $\lambda/20$ ($\approx$5mm pitch) was utilised to avoid 'faceting' of the geometry for this reason. The mesh can be seen in Fig 5.
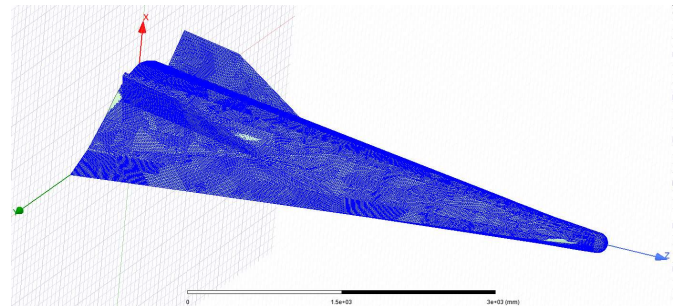

Fig 5 Surface mesh utilised for PO solver at S-band.

Note that the vehicle representation is shown with a z-oriented long axis, using a conventional right-handed co-ordinate system. In subsequent discussions regarding the datasets, θ is thus defined as going from the z-axis in the direction of the x-axis, whilst φ extends from x to y in the conventional manner.

3. Running the Solver and Extracting Results.

Simulation at a single spot frequency required around 2GB of RAM and four hours per run across 8 Intel Xeon cores, a single run providing results for one polarisation.

The resultant RCS was obtained in 5° steps over 0°≤θ≤360° and 0°≤φ≤180°. These are essentially cuts akin to the segments of an orange moving from the nose of the vehicle to the tail. A φ=90° cut thus represents a range of azimuth angles around the vehicle at zero elevation in a clockwise direction, whilst a φ=0° cut moves vertically around the vehicle body (in the xz-plane; for co-ordinate system see figures.).

Monostatic RCS values are presented for VV and HH polarisation cases in Fig. 6 and Fig. 7. There is little difference between the results derived from the two different polarisations because the object is electrically large (the target is in the 'optical regime') and therefore diffraction only represents a small contribution to the overall RCS.

The full datasets were imported into Matlab and processed to show surface plots, Fig. 8 and Fig 9.
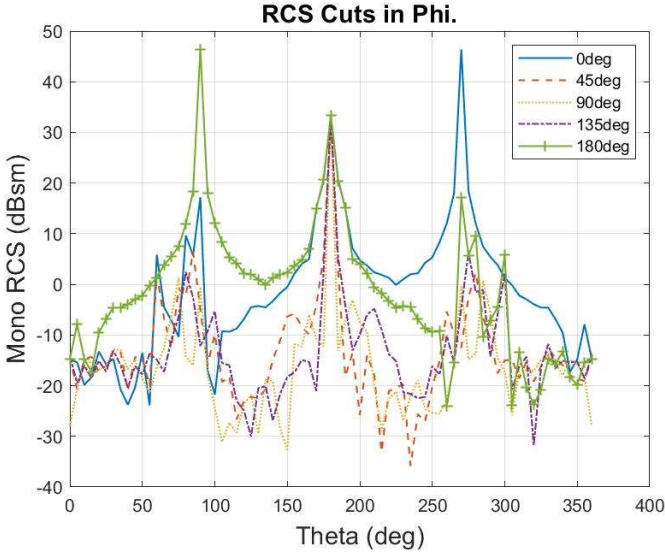
Fig. 6 VV polarisation cuts in φ around the body of the vehicle. Large spikes at φ=90/270deg are due to the flat 'bottom' and for φ=180deg, rear.
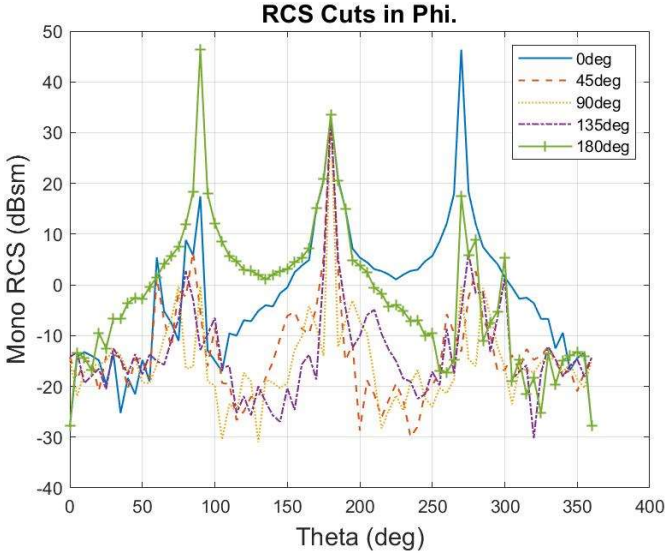

Fig. 7 HH polarisation cuts around the body. There is little difference in RCS values for the two polarisation cases.

The 5° sampling interval is larger than the Nyquist angular sampling interval, in radians, given in equation (i).

$$\boldsymbol{\theta_N} \approx \frac{\lambda}{4r_{max}} \qquad \text{(i)}$$

This equates to ≈0.6° at S-band, r_{max} being the maximum radius of a point on a sphere enclosing the geometry, approximately half its length (2.5m) in this instance (the factor of 4 occurs because backscatter involves a 'round-trip' path to and from the target). However, Nyquist sampling of a full 3D scattered field was found to be impractical without additional computing resources (a run time of >1 week for the full dataset).

The strong return at θ = 180° for all φ angles is a consequence of the high RCS presented by the target viewed from the rear

aspect. The other 'flashes' near θ=90° and θ=270° for φ=180° and φ=0°, respectively, are a consequence of the planar underside. Other flashes are likely due to specular reflections from the nose and fins.
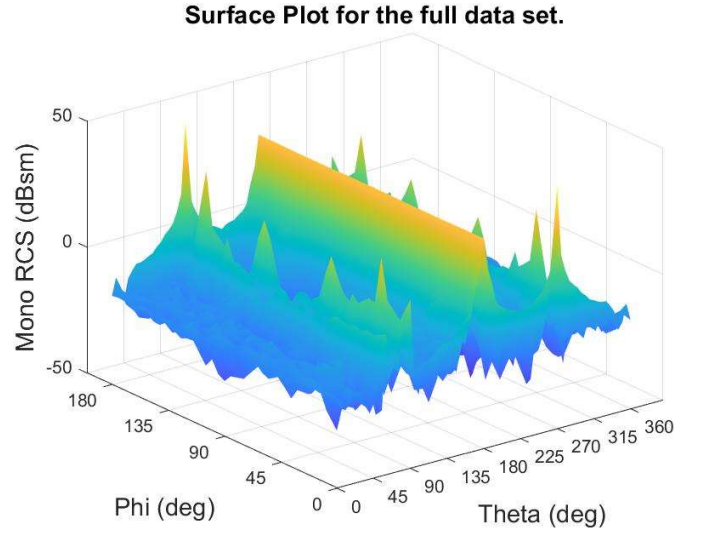

Fig. 8 Surface plot for the full Mono RCS dataset, VV-polarisation.
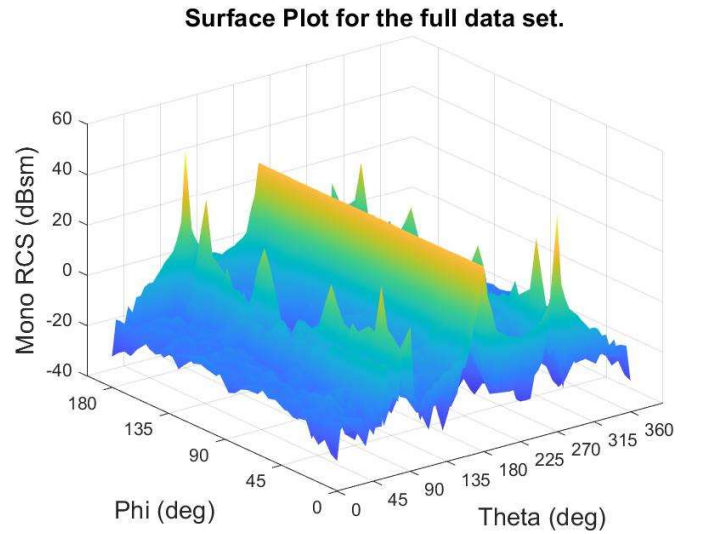

Fig 9 Surface plot for the full Mono RCS dataset, HH-polarisation.

The resultant data represents a full sphere of monostatic RCS values. The Matlab script was extended to allow histograms to be produced based on data over a limited range of viewing angles, selectable by varying the extent of θ utilised. Allowing all angles to be included is essentially akin to assuming that the vehicle is tumbling (or otherwise manoeuvring rapidly through the full angular range) between samples, which is not particularly realistic. Consequently, some assumption must be made regarding the range of viewing angles likely to be presented to the radar over the maximum dwell period.

3

The range chosen was $-30^\circ \leq \theta \leq +30^\circ$, with all φ values being included. This equates to 13 θ and 37 φ angles, giving a total of 481 data points. In essence, we are assuming that a range of angles equal to 60° about the nose of the vehicle, in any plane, may be presented to the radar. The resultant histogram is displayed in Fig. 10 for VV polarisation. The HH polarisation case is shown in Fig. 11 and shows a very similar spread of values of RCS. 40 bins were selected, this number being chosen to be a compromise between showing the shape of the distribution and ensuring a reasonable number of samples in each bin.
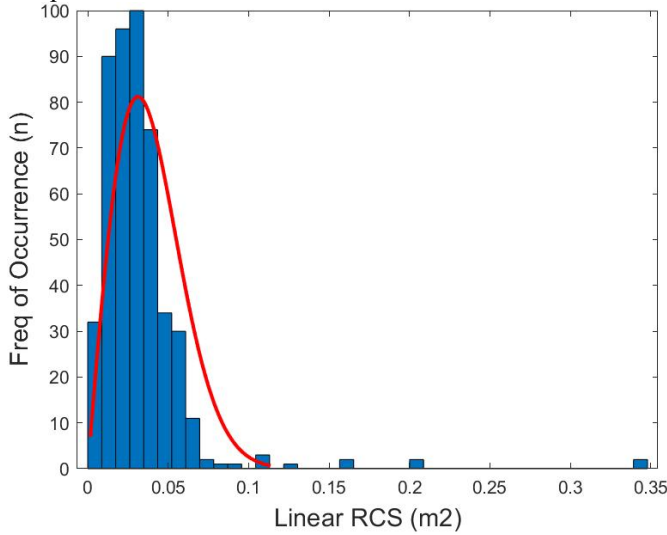

Fig. 10 VV polarisation case histogram, based on viewing angle over all φ, $-30^\circ \leq \theta \leq +30^\circ$, with normalised Rayleigh distribution overlaid.
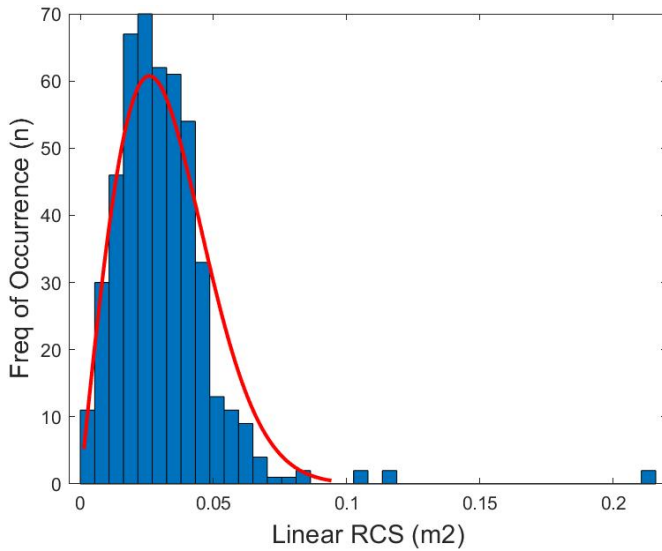

Fig. 11 HH polarisation case histogram, as with the VV data, a normalised Rayleigh distribution was found to offer a good fit to the all φ, $-30^\circ \leq \theta \leq +30^\circ$ data.

It was subsequently found that a Rayleigh distribution offered an appropriate fit to both VV and HH polarisation data. The fit is shown overlaid on the histograms in Fig. 10 and Fig. 11. In both instances, the 'histfit' command was utilised in Matlab. The distribution is normalised to the area under the

histogram. The resultant probability density function thus takes the form given by:-

$$f(x, \sigma) = \frac{x}{\sigma^2} e^{\frac{-x^2}{2\sigma^2}} \text{ (ii)}$$

σ is the scale parameter, and is a measure of the spread of the distribution. It is calculated for the distribution using:-

$$\sigma = \sqrt{\frac{1}{2n} \sum_{i=1}^{n} x_i^2} \text{ (iii)}$$

Where n is the number of samples and x_i is the value of the ith sample.

For the distributions fitted, the key parameters are given in Table 1.

Data	Scale Parameter (σ)	Mean (μ)	Stdev (RCS/m^2)	Lower limit (RCS/m^2)	Upper limit (RCS/m^2)
VV – Pol'n	0.031	0.039	0.021	0.007	0.085
HH – Pol'n	0.026	0.032	0.017	0.006	0.070

Table 1 Key distribution parameters for dataset fits.

Note that a regular point of confusion is that σ is often used to represent the distribution's spread or 'Scale Parmeter' as mentioned above, but it also commonly represents RCS in the radar range equation. In the notation used in the distribution equations, σ is the scale parameter, whilst x is used to represent the RCS value being sampled. This has been done deliberately to avoid confusion.

In Table 1, the Lower and Upper limits correspond to the 95% confidence intervals for Rayleigh distributions (i.e. the values between which 95% of randomly sampled RCS values would fall).

It is interesting to see how these Rayleigh distributions compare with the more commonly used Swerling forms typically applied to represent target fluctuations. Swerling 1&2 are represented by the functions below [11]:-

$$f(x, \sigma) = \frac{1}{\sigma} e^{\frac{-x}{\sigma}} \text{ (iv)}$$

Whilst Swerling 3 and 4 are described by:-

$$f(x, \sigma) = \frac{4x}{\sigma^2} e^{\frac{-2x}{\sigma}} \text{ (v)}$$

These functions are compared against the Rayleigh distribution fitted to the histogram dataset in Fig. 12 (VV) and Fig. 13 (HH). They have each been normalised such that the area under the curves remain the same.
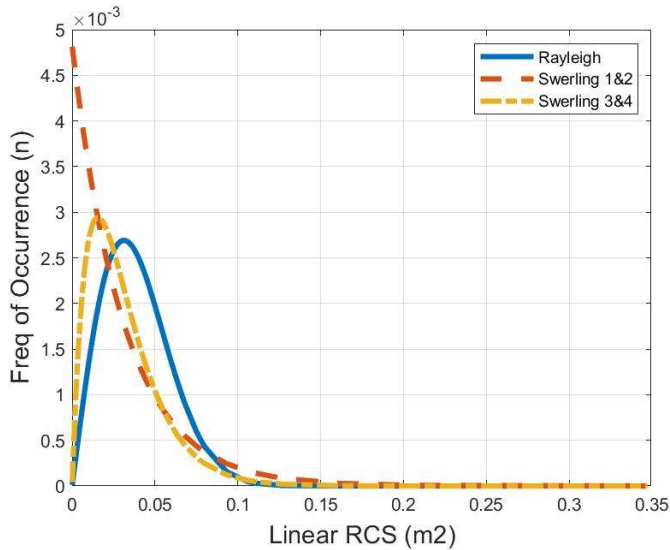
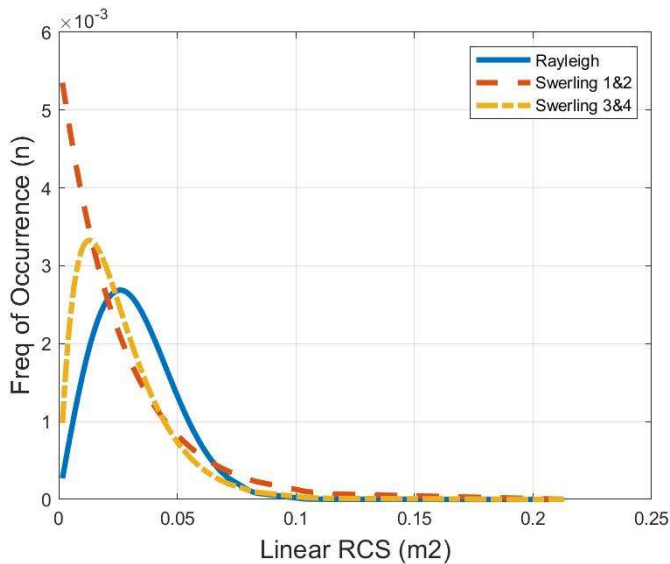**Fig. 12 Comparison of normalised distributions - VV**

Fig. 13 Comparison of normalised distributions - HH

The results demonstrate that a Swerling 1&2 type distribution (Chi squared with two degrees of freedom (DOF), m=1, resulting in an exponential distribution) is clearly not appropriate for this dataset, but that the Swerling 3&4 (Chi squared with four DOF, m=2) is a rather better approximation. Even for this latter case, it can be seen that the distribution peak is at too low a value in *x* to correspond to the modal average of the dataset (i.e. the *x*-axis value at which the peak of the histogram occurs), making the Rayleigh a better approximation.

It is unsurprising that the Swerling 3&4 cases are reasonably applicable, since they physically represent situations where one major scatterer is accompanied by several minor ones. In this instance this corresponds to scattering from the vehicle's nose, together with returns from the fins and other minor scatterers over the range of viewing angles sampled.

It is also worthwhile attempting to make some form of assessment of the fit associated with the distribution to the

actual dataset. This can be readily achieved by calculating the cumulative density function (CDF), obtained by integrating under the probability density function (PDF) curve. This can be compared with a CDF for our histogram data, and also allows the RMS figure for the difference to be computed to quantitatively define the quality of the fit. A good fit will thus have a low RMS difference. The CDFs for the histogram, fitted distribution, and the Swerling 3&4 case, are shown for the two polarisations in Fig. 14 and Fig. 15.
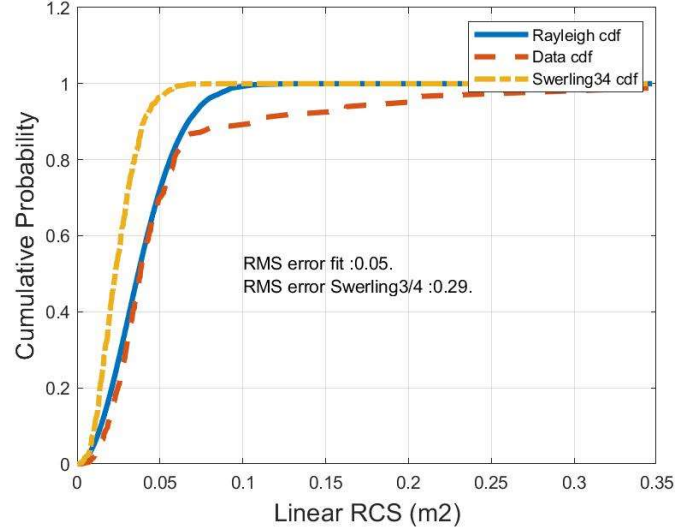

Fig. 14 Cumulative Density Function for data, fit, and Chi Squared m=2, VV-pol.
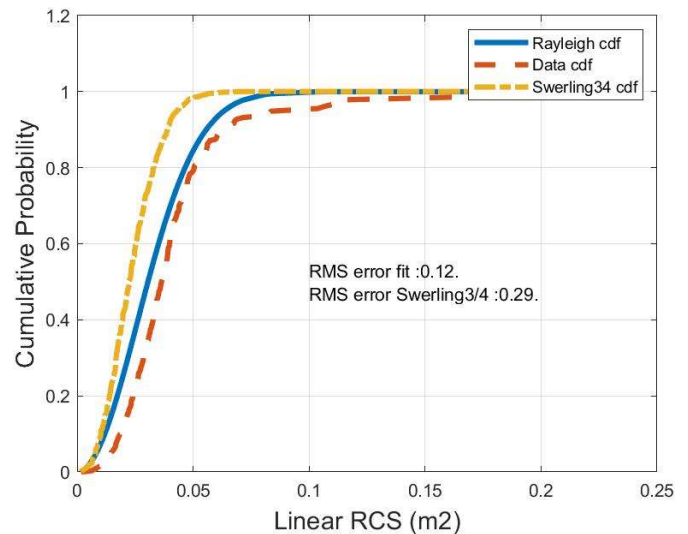

Fig. 15 Cumulative Density Function for data, fit, and Chi Squared m=2, HH-pol.

Inspection of Fig. 14 shows that the Rayleigh distribution (blue solid curve) is a better approximation to the data CDF curve (red dashed) than the Chi Squared m=2 distribution (yellow dot-dash curve) associated with the Swerling 3&4 cases. The RMS error figure for the Rayleigh fit is correspondingly lower than for the Chi Squared m=2 case. The Fig. 15 (HH) results support the same conclusion.

4. Effect on Maximum Detection Range.

The effect of using the two different representations of a fluctuating HGV target's statistical behaviour on P_d, SNR and ultimately maximum detection range (R_{max}) was further investigated. The Rayleigh and Swerling III distributions were re-expressed, such that the random variable and scale factors are given in terms of the Signal to Noise Ratio (SNR), γ within the detector and mean SNR, $\bar{\gamma}$.

$$\boldsymbol{\gamma} = \frac{\sigma}{2\sigma_n^2} \ \text{(vi)}$$

In eqn.(vi), $\sigma/2$ represents signal power and σ_n^2 noise power. Reference [12], describes the equation for the PDF of a constant target in noise through a square law detector as a function of γ. For our case, we treat this as a conditional PDF and use the Rayleigh distribution, now also in terms of γ, to give the overall PDF for the square law detector output.

$$\boldsymbol{P_d(\theta, \gamma)} = \int_\theta^\infty \int_0^\infty \boldsymbol{p(y|\gamma)} \cdot \frac{\pi\gamma}{2\bar{\gamma}} \boldsymbol{e}^{-\frac{\gamma^2\pi}{4\bar{\gamma}^2}} \cdot \boldsymbol{d\gamma} \cdot \boldsymbol{dy} \ \text{(vii)}$$

Note that θ is the detection threshold for a given P_{fa}; where P_{fa} is the probability of false alarm and y is the decision statistic for power law detection. Applying this gives the curve shown in Fig. 16.
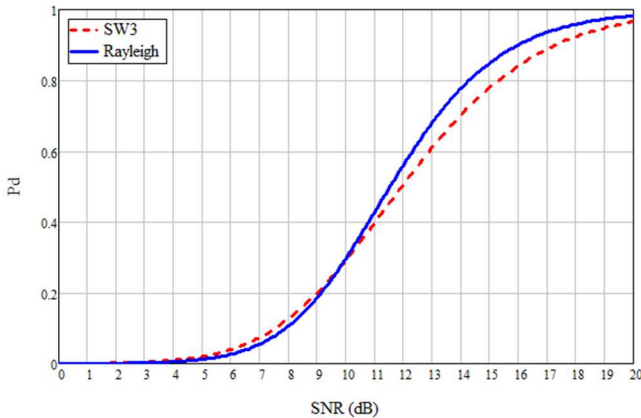

Fig. 16 Comparison of P_d curves for Swerling III and Rayleigh.

As can be observed from Fig. 16, at a P_d of 0.8, the difference in SNR is approximately 1dB less, relative to Swerling III. For SNRs≥10dB, a smaller SNR is thus required to achieve a given P_d. This translates through to an increase in maximum detection range, R_{max}, of around 6% using a Rayleigh based representation, relative to Swerling III. Whether this is significant will depend upon the particular use-case.

5. Conclusions.

As might be anticipated, since it was developed to represent cases where a single dominant scatterer is accompanied by several smaller scatterers, the Chi-squared with m=2 distribution classically used to represent Swerling III/IV targets was found to offer a good representation of HGV backscatter behaviour. This assumed that the glide body was manoeuvring in any plane over a ±30° angular range from the vehicle's nose (essentially a uniform distribution with all angles being equally probable). It also assumed that the target was in the 'optical' scattering regime, being electrically large. A Rayleigh distribution was demonstrated to offer an improved representation of HGV behaviour, but this only translated to around a 6% difference in the estimation of R_{max}, at an SNR well above 10dB. Whether the additional effort of employing a custom distribution is worthwhile will depend on the specifics of particular use-cases, and the fidelity of the output required.

5 Acknowledgements

6 References

[1] Swerling P. : "Probability of Detection for Fluctuating Targets", USAF Project, RAND Research Memorandum, RM-1217, AD80638, 17th March 1954.

[2] Marcum, J. I. : "A Statistical Theory of Target Detection by Pulsed Radar", The RAND Corporation, Research Memorandum RM-7, December 1, 1947."

[3] Wikipedia Article : "Ballistic Missile" - https://en.wikipedia.org/wiki/Ballistic_missile - Accessed 23rd March 2022.

[4] Wikipedia Article : "List of Missiles" - https://en.wikipedia.org/wiki/List_of_missiles - Accessed 23rd March 2022.

[5] Military Today Article : "DF-17" - http://www.military-today.com/missiles/df_17.htm - Accessed 23rd March 2022.

[6] BBC News Article : "Russia Deploys Avangard Hypersonic Missile System" - https://www.bbc.co.uk/news/world-europe-50927648 - Accessed 23rd March 2022.

[7] Aerosociety News Article : "From Sanger to Avangard – Hypersonic Weapons Come of Age" - https://www.aerosociety.com/news/from-saenger-to-avangard-hypersonic-weapons-come-of-age/ Accessed 11th March 2022.

[8] Wikipedia Article : "RS-28 'Sarmat'" - https://en.wikipedia.org/wiki/RS-28_Sarmat - Accessed 11th March 2022.

[9] Wikipedia Article : "Trident (Missile)" - https://en.wikipedia.org/wiki/Trident_(missile) – Accessed 11th March 2022.

[10] Pinto J. : "The RCS of (name withheld)", BAE Systems Technical Memorandum, Ref. AIL2174, Oct. 2017.

[11] Wikipedia Article : "Fluctuation Loss" - https://en.wikipedia.org/wiki/Fluctuation_loss - Accessed 14th March 2022.

[12] Middlestead Richard W., "Digital Communications with Empasis on Data Modems : Theory, Analysis, Design, Simulation, Testing and Applications", First Ed. John Wiley and Sons, 2017, Appendix C – Detection of Signals in Noise.